NASA Technical Memorandum 88362

Calculation of External-Internal Flow Fields for Mixed-Compression Inlets

W. J. Chyu,
T. Kawamura,
D. P. Bencze, Ames Research Center, Moffett Field, California

October 1986

National Aeronautics and
Space Administration

Ames Research Center
Moffett Field, California 94035

CALCULATION OF EXTERNAL-INTERNAL FLOW FIELDS FOR MIXED-COMPRESSION INLETS

W.J. Chyu, T. Kawamura, and D.P.Bencze
NASA Ames Research Center, Moffett Field, California

Abstract

Supersonic inlet flows with mixed external-internal compressions were computed using a combined implicit-explicit (Beam-Warming-Steger/MacCormack) method for solving the three-dimensional unsteady, compressible Navier-Stokes equations in conservation form. Numerical calculations were made of various flows related to such inlet operations as the shock-wave intersections, subsonic spillage around the cowl lip, and inlet 'started' versus 'unstarted' conditions. Some of the computed results were compared with wind tunnel data.

Introduction

The design of the inlet system is a critical part of the design of the entire propulsion system. For advanced supersonic aircraft, integrated design procedures are required which can account for both the external and internal flow fields. Although a great deal of numerical study has been focused on purely internal flows, there have been few computational studies of complete inlet systems such as shown in Figure 1.

The analysis of mixed compression inlet flows is complicated by the formation of multiple shock waves that are generated in the external flow field by the external compression surfaces (ramps, centerbodies, aircraft forebodies) and the cowl, and in the internal flow field from the cowl lip to the engine face. For subcritical flow (or supercritical and critical flows with flow incidence), the analysis must be able to treat both the external and internal flow fields to accurately predict the cowl spillage. Internally, the analysis must be able to treat shock wave boundary layer interactions and shock wave intersections. In addition, for practical inlet analyses the three dimensional effects due to angle of attack and nonuniform freestream must also be included in the analyses.

Numerical analysis of mixed-compression inlets was led by the development of spatial marching algorithms based on two-dimensional method of characteristics.[1-4]

Presented at First World Congress on Computational Mechanics, Austin, Texas, September 22-26, 1986.

Recently the characteristic method with discrete shock wave-fitting technique[4] was combined with solutions of the boundary-layer equations to account for the viscous effects which dominate inlet flow fields.[5] A similar method, but combined with a three-dimensional swept shock interaction technique,[6] has been also reported. These methods demonstrated the efficient capability of computing three-dimensional mixed compression inlets, but were limited to the supersonic portion of the flow field and were incapable of treating the terminal shock and the subsonic flow at the engine face.

Another approach for treating the inlet flow problem is to use the finite-difference solution to the full potential equation. The computational methods involve a conformal mapping technique,[7] and a sequence of simpler transformations,[8] to transform the flow equation to a boundary conforming coordinate system. The potential equation can also be solved in Cartesian[9,10] as well as in generalized[11] coordinates. These computational methods have been shown to be fast and stable, but cannot account for the important viscous effects.

The complicated flows of mixed compression inlets are amenable to computation by solving the Navier-Stokes equations. One of the approaches taken in this effort was the use of the MacCormack explicit scheme[12] in developing a shock-capturing algorithm for the solution of a supersonic inviscid flow,[13] and in solving the noniterative shock-capturing parabolized Navier-Stokes algorithm.[14] Recently, the MacCormack explicit algorithm was further applied to the computations of two-dimensional high speed inlets[15-17] and a three-dimensional axisymmetric inlet with[18] and without[19] angle of attack. The development of an efficient explicit code has been, however, hampered by the restriction on the maximum time intervals required for numerical stability.

As opposed to the explicit approach, an implicit algorithm of the alternating-direction, implicit (ADI) finite difference scheme[20,21] permits larger time intervals for integration. The usage of the ADI scheme in conjunction with a diagonal implicit method,[22] a finite-volume formulation[23], and implicit and hybrid methods[24] has resulted in the computations of a two-dimensional external compression inlet flow field.

The purpose of this study is to develop an efficient numerical technique for accurately analyzing a three-dimensional mixed compression inlet flow field. Toward this end, a combined implicit-explicit approach is adopted for solving the unsteady, compressible Navier-Stokes equations in conservation form. The implicit part of the algorithm adopts the alternating-direction scheme[20,21] to integrate the continuity and energy equations and both the momentum equations in streamwise (ξ) and normal (η) directions; whereas the explicit part adopts the MacCormack predictor-corrector scheme[12] in the azimuthal (Θ) momentum integration.

The selection of the combined implicit-explicit method is based on concerns

over accuracy and computational efficiency of the resulting code. The inlet analysis requires a finely spaced grid in the boundary layer (or in the inlet wall region) to resolve the strong shock-wave/boundary-layer interactions and potential flow separations. The inherently stable implicit scheme capable of accommodating large time steps is suitable for carrying out the ADI integration across the densely distributed grid points in the boundary layer in the η direction. In contrast to the implicit method, the explicit method (in which the numerical stability mandates the maximum allowable time step to be dependent on the smallest spatial scale) cannot efficiently handle the integration across the boundary layer. Explicit methods, however, can be effectively used in the azimuthal integration wherein flow variation is relatively minor and the fine grid clustering, as in the boundary layer, is not necessary.

In the following sections, the numerical technique is described for applying this approach in solving the Navier-Stokes equations, the computed results are presented for various flow conditions, and some comparisons are made with available wind-tunnel data.

Numerical Technique

Governing Equations

The flow is assumed to follow the full, unsteady, compressible, Navier-Stokes equations in conservation form:

$$\begin{aligned} \rho_{,t} + (\rho V_i)_{,i} &= 0 \\ (\rho V_i)_{,t} + \Omega_{ij,j} &= 0 \\ e_{,t} + \Lambda_{i,i} &= 0 \end{aligned}$$

where

$$\begin{aligned} \Omega_{ij} &= \rho V_i V_j + p\delta_{ij} - \tau_{ij} \\ \Lambda_i &= (e+p)V_i + q_i - \tau_{ij}V_j \end{aligned}$$

Here, ρ, V, e, and p denote density, velocity, energy, and pressure, respectively; q and τ denote heat transfer and skin friction, respectively.

The governing equations in cylindrical coordinates can be expressed as

$$\partial_t \mathbf{U} + \partial_r \mathbf{E} + \partial_\theta \mathbf{F} + \partial_z \mathbf{G} = -\mathbf{H}$$

where

$$\mathbf{U} = \begin{pmatrix} \rho \\ \rho u_r \\ \rho u_z \\ e \\ \rho u_\theta \end{pmatrix}, \qquad \mathbf{E} = \begin{pmatrix} \rho u_r \\ \Omega_{rr} \\ \Omega_{rz} \\ \Lambda_r \\ \Omega_{r\theta} \end{pmatrix}, \qquad \mathbf{F} = \frac{1}{r}\begin{pmatrix} \rho u_\theta \\ \Omega_{r\theta} \\ \Omega_{\theta z} \\ \Lambda_\theta \\ \Omega_{\theta\theta} \end{pmatrix},$$

$$\mathbf{G} = \begin{pmatrix} \rho u_z \\ \Omega_{rz} \\ \Omega_{zz} \\ \Lambda_z \\ \Omega_{z\theta} \end{pmatrix}, \qquad \text{and} \qquad \mathbf{H} = \frac{1}{r}\begin{pmatrix} \rho u_r \\ \Omega_{rr} - \Omega_{\theta\theta} \\ \Omega_{rz} \\ \Lambda_r \\ 2\Omega_{r\theta} \end{pmatrix}$$

The skin friction in terms of the cylindrical coordinates gives a form

$$\begin{aligned}
\tau_{rr} &= 2\mu\partial_r u_r + \lambda(\partial_r u_r + \partial_\theta u_\theta/r + u_r/r + \partial_z u_z) \\
\tau_{zz} &= 2\mu\partial_z u_z + \lambda(\partial_r u_r + \partial_\theta u_\theta/r + u_r/r + \partial_z u_z) \\
\tau_{\theta\theta} &= 2\mu(\partial_\theta u_\theta/r + u_r/r) + \lambda(\partial_r u_r + \partial_\theta u_\theta/r + u_r/r + \partial_z u_z) \\
\tau_{rz} &= \tau_{zr} = \mu(\partial_z u_r + \partial_r u_z) \\
\tau_{r\theta} &= \tau_{\theta r} = \mu(\partial_r u_\theta - u_\theta/r + \partial_\theta u_r/r) \\
\tau_{\theta z} &= \tau_{z\theta} = \mu(\partial_\theta u_z + \partial_z u_\theta)
\end{aligned}$$

wherein the Stokes hypothesis $\lambda + (2/3)\mu = 0$ is assumed.

To obtain flow solutions on a body-conforming grid that is suitable for treating an arbitrary inlet geometry and implementing the necessary flow boundary conditions, a generalized transformation is applied to the governing equations using a form $\xi = \xi(z, r, \theta, t)$, $\eta = \eta(z, r, \theta, t)$, $\Theta = \Theta(z, r, \theta, t)$, and $\tau = t$. The resulting flow equations give the form

$$\partial_\tau \hat{\mathbf{U}} + \partial_\xi \hat{\mathbf{P}} + \partial_\eta \hat{\mathbf{Q}} + \partial_\Theta \hat{\mathbf{R}} = -\hat{\mathbf{H}} \tag{1}$$

where

$$\begin{aligned}
\hat{\mathbf{U}} &= \mathbf{U}/\mathbf{J} \\
\hat{\mathbf{P}} &= \xi_t \hat{\mathbf{U}} + \xi_r \tilde{\mathbf{E}} + \xi_\theta \tilde{\mathbf{F}} + \xi_z \tilde{\mathbf{G}} \\
\hat{\mathbf{Q}} &= \eta_t \hat{\mathbf{U}} + \eta_r \tilde{\mathbf{E}} + \eta_\theta \tilde{\mathbf{F}} + \eta_z \tilde{\mathbf{G}} \\
\hat{\mathbf{R}} &= \Theta_t \hat{\mathbf{U}} + \Theta_r \tilde{\mathbf{E}} + \Theta_\theta \tilde{\mathbf{F}} + \Theta_z \tilde{\mathbf{G}} \\
\hat{\mathbf{H}} &= \mathbf{H}/\mathbf{J}
\end{aligned}$$

and $\mathbf{J}$ denotes the Jacobian,

$$\mathbf{J}^{-1} = \xi_z\eta_r\Theta_\theta + \xi_r\eta_\theta\Theta_z + \xi_\theta\eta_z\Theta_r - \xi_\theta\eta_r\Theta_z - \xi_r\eta_z\Theta_\theta - \xi_z\eta_\theta\Theta_r$$

Here, it is denoted that $\tilde{\mathbf{E}} = \mathbf{E}/\mathbf{J}$, $\tilde{\mathbf{F}} = \mathbf{F}/\mathbf{J}$, and $\tilde{\mathbf{G}} = \mathbf{G}/\mathbf{J}$. The first row of vector Equation (1) corresponds to the equation of continuity. Likewise the second and third rows are the momentum equations in the ξ and η directions, respectively, while the fourth row is the energy equation and the fifth row is the momentum equation in the Θ direction.

Finite Difference Procedure

The first four rows of Equation (1) are integrated in time, subject to appropriate initial and boundary conditions, using the Beam-Warming-Steger alternating-direction, implicit (ADI) scheme.[20,21] The last row of Equation (1), the momentum equation in the Θ direction, is integrated in time with the MacCormack explicit scheme[12] using the newly computed values (from the ADI scheme) of density, energy, and velocities in the ξ and η directions.

To apply the ADI scheme in the ξ and η directions, the first four rows of Equation (1) are arranged in the following form.

$$\partial_\tau \hat{\mathbf{U}} + \partial_\xi \hat{\mathbf{P}}_i + \partial_\eta \hat{\mathbf{Q}}_i = \hat{\mathbf{S}} \tag{2}$$

where

$$\hat{\mathbf{S}} = -\hat{\mathbf{H}}_i - \partial_\Theta \hat{\mathbf{R}}_i - Re^{-1}(\partial_\xi \hat{\mathbf{P}}_v + \partial_\eta \hat{\mathbf{Q}}_v + \partial_\Theta \hat{\mathbf{R}}_v + \hat{\mathbf{H}}_v)$$

As opposed to the terms $\hat{\mathbf{P}}_i$, $\hat{\mathbf{Q}}_i$, $\hat{\mathbf{R}}_i$, and $\hat{\mathbf{H}}_i$, which contain only the inviscid flux terms, the terms $\hat{\mathbf{P}}_v$, $\hat{\mathbf{Q}}_v$, $\hat{\mathbf{R}}_v$, and $\hat{\mathbf{H}}_v$, contain the remaining viscous derivatives and heat transfer terms.

In the Beam-Warming-Steger delta-form ADI algorithm, Equation (2) can be written as

$$\begin{aligned}
&[\,\mathbf{I} + h\delta_\xi(\hat{\mathbf{A}} - \delta_\xi \hat{\mathbf{K}})^n - \mathbf{J}^{-1}\alpha h \nabla_\xi \Delta_\xi \mathbf{J}\,] \\
&\qquad \times [\,\mathbf{I} + h\delta_\eta(\hat{\mathbf{B}} - \delta_\eta \hat{\mathbf{L}})^n - \mathbf{J}^{-1}\alpha h \nabla_\eta \Delta_\eta \mathbf{J}\,](\hat{\mathbf{U}}^{n+1} - \hat{\mathbf{U}}^n) \\
&= \Delta\tau(-\partial_\xi \hat{\mathbf{P}}_i - \partial_\eta \hat{\mathbf{Q}}_i + \hat{\mathbf{S}})^n - \alpha h \mathbf{J}^{-1}[\,(\nabla_\xi \Delta_\xi)^2 + (\nabla_\eta \Delta_\eta)^2\,]\mathbf{J}\hat{\mathbf{U}}^n
\end{aligned} \tag{3}$$

where second-order time differencing, $h = \Delta\tau/2$, and second-order central difference for the convection terms, δ_ξ and δ_η, are used in the computation. It is noted here that $\hat{\mathbf{P}}_v$ and $\hat{\mathbf{Q}}_v$ are divided into two parts, one containing ξ and the other η derivatives; that is

$$\begin{aligned}
\hat{\mathbf{P}}_v(\hat{\mathbf{U}}, \hat{\mathbf{U}}_\xi, \hat{\mathbf{U}}_\eta) &= \hat{\mathbf{P}}_{v1}(\hat{\mathbf{U}}, \hat{\mathbf{U}}_\xi) + \hat{\mathbf{P}}_{v2}(\hat{\mathbf{U}}, \hat{\mathbf{U}}_\eta) \\
\hat{\mathbf{Q}}_v(\hat{\mathbf{U}}, \hat{\mathbf{U}}_\xi, \hat{\mathbf{U}}_\eta) &= \hat{\mathbf{Q}}_{v1}(\hat{\mathbf{U}}, \hat{\mathbf{U}}_\xi) + \hat{\mathbf{Q}}_{v2}(\hat{\mathbf{U}}, \hat{\mathbf{U}}_\eta)
\end{aligned}$$

$\hat{\mathbf{K}}$ and $\hat{\mathbf{L}}$ [20,25] are defined as $\hat{\mathbf{K}} \equiv \partial_{\hat{\mathbf{U}}_\xi} \hat{\mathbf{P}}_{v1}$, and $\hat{\mathbf{L}} \equiv \partial_{\hat{\mathbf{U}}_\eta} \hat{\mathbf{Q}}_{v2}$. $\hat{\mathbf{A}}$ and $\hat{\mathbf{B}}$[21] result from the local linearization of the fluxes about the previous time level as given by $\hat{\mathbf{A}} \equiv \partial_{\hat{\mathbf{U}}} \hat{\mathbf{P}}_i$ and $\hat{\mathbf{B}} \equiv \partial_{\hat{\mathbf{U}}} \hat{\mathbf{Q}}_i$. Fourth order dissipation terms $(\nabla_\xi \Delta_\xi)^2$ and $(\nabla_\eta \Delta_\eta)^2$ are added to the right-hand side of Equation (3) to control the numerical stability.[21] The spatial derivatives $\partial_\xi \hat{\mathbf{P}}_{v2}$ and $\partial_\eta \hat{\mathbf{Q}}_{v1}$ involve cross derivatives $\partial_\xi \partial_\eta \hat{\mathbf{U}}_\xi$ and $\partial_\xi \partial_\eta \hat{\mathbf{U}}_\eta$; in order to use a spatially factored scheme, these terms can be time lagged to an $n-1$ time level. These terms were neglected in the present computation, which reduces the order of the time-accuracy in the computation of dissipation terms from second to first order. For an axisymmetric body (the flow need not necessarily be axisymmetric), the transformations $\xi = \xi(z, r), \eta = \eta(z, r)$ and $\Theta = \theta$ give $\Theta_\theta = 1$ and $\xi_\theta = \eta_\theta = 0$. With this transformation, the Jacobian is reduced to $\mathbf{J} = \Theta_\theta \mathbf{J}_z = \mathbf{J}_z$, where $\mathbf{J}_z$ denotes the two-dimensional Jacobian, $\mathbf{J}_z = \xi_z \eta_r - \xi_r \eta_z$. The expressions for terms $\hat{\mathbf{P}}, \hat{\mathbf{Q}}, \hat{\mathbf{R}}$, and $\hat{\mathbf{H}}$ can also be greatly simplified. The left-hand-side Equation (3) can be factored in ξ and η components and solved by sweeping in each direction by inverting tridiagonal matrices of 4×4 blocks.

The original MacCormack scheme[12] is applied to the last row of Equation (1) or the momentum equation in Θ direction, using the algorithm :

Predictor:

$$\begin{aligned}\hat{\mathbf{U}}^{\overline{n+1}}_{j,k,l} =& \hat{\mathbf{U}}^n_{j,k,l} - h_1(\hat{\mathbf{P}}^n_{j+1,k,l} - \hat{\mathbf{P}}^n_{j,k,l}) - h_2(\hat{\mathbf{Q}}^n_{j,k+1,l} - \hat{\mathbf{Q}}^n_{j,k,l}) \\ & - h_3(\hat{\mathbf{R}}^n_{j,k,l+1} - \hat{\mathbf{R}}^n_{j,k,l}) - h_0 \hat{\mathbf{H}}^n_{j,k,l}\end{aligned}$$

Corrector:

$$\begin{aligned}\hat{\mathbf{U}}^{n+1}_{j,k,l} =& 1/2\big[\hat{\mathbf{U}}^n_{j,k,l} + \hat{\mathbf{U}}^{\overline{n+1}}_{j,k,l} - h_1(\hat{\mathbf{P}}^{\overline{n+1}}_{j,k,l} - \hat{\mathbf{P}}^{\overline{n+1}}_{j-1,k,l}) - h_2(\hat{\mathbf{Q}}^{\overline{n+1}}_{j,k,l} - \hat{\mathbf{Q}}^{\overline{n+1}}_{j,k-1,l}) \\ & - h_3(\hat{\mathbf{R}}^{\overline{n+1}}_{j,k,l} - \hat{\mathbf{R}}^{\overline{n+1}}_{j,k,l-1}) - h_0 \hat{\mathbf{H}}^{\overline{n+1}}_{j,k,l}\big]\end{aligned}$$

where $h_0 = \Delta\tau$, and $h_1 = \Delta\tau/\Delta\xi$, $h_2 = \Delta\tau/\Delta\eta$, and $h_3 = \Delta\tau/\Delta\Theta$, and $\xi = j\Delta\xi$, $\eta = k\Delta\eta$, and $\Theta = l\Delta\Theta$.

Grid-Generation and Boundary Condition

Since the flow structures vary greatly in both the external and internal flow fields, the grid is divided into two zones; one covers mainly the external (freestream) region and the other the internal (inlet) region of the flow field (Figure 1). The outer boundary points of the external zone are specified with a uniform grid spacing. The inner boundary points, however, are specified with grid spacing clustered in the regions near the tip of the centerbody and the cowl lip, and the inlet wall in the throat region.

Once the grid is specified on its boundaries, an elliptic solver[26] can be used to generate a smoothly spaced grid at the interior points in each zone of the flow field. H-grid is used in each zone to properly describe the centerbody and the sharp cowl lip. The interior of the grid is densely clustered in the boundary layer to account for the rapid flow variation and the shock-wave/boundary-layer (or shock wave/inlet wall) interactions. H-grids generated in the internal and external zones share common boundary points along a $\eta = constant$ line extending from the cowl lip to the upstream boundary.

The computations were performed on a grid consisting of two zones which share a strip of grid points on the common boundary extending from the cowl lip to the upstream boundary. The computations were carried out in each zone interchangeably, and the computed data in each zone were stored in a solid state disk for the next step iteration. Two zones of the flow field were coupled along the common boundary where, prior to initiating the computation on each zone, the boundary conditions were updated. This was done by taking the average of the flow quantities that had been computed on the grid points on the $\eta = constant$ lines directly above and below the common boundary.

On the outer boundary of the grids, free-stream conditions are applied. Along the body surface of the centerbody and cowl, the tangency condition is imposed for the inviscid flow computations; for the viscous flow, the no-slip condition is imposed. An engine face static pressure at the inlet exit was imposed on the boundary using an explicit boundary treatment.[27]

Results

An existing experimental mixed compression axisymmetric inlet model[28] with a translating cowl was selected for analysis because of the extensive amount of data available for comparison. The inlet was tested in the 8- by 7-, 9- by 7-, and 11- by 11-Foot Wind Tunnels at Ames Research Center over the Mach number range 0.6 to 2.65. The internal contours, designed for Mach number 2.65, provided a throat area equal to 59 % of the capture area when the centerbody was retracted for supersonic operation. The experimental data were taken at a tunnel total pressure of about 1 atm (a unit Reynolds number of about $8.53 \times 10^6/m$ at Mach number 2.65). The experimental data included total pressure recovery and static-pressure distributions along both the centerbody and cowl for various bleed configurations and mass flow ratios. At the design Mach number 2.65, the conical shock from the centerbody sits slightly ahead of the cowl lip. This Mach number was chosen for computing the inlet flow field at critical condition (an inlet at 'started' condition with terminal shock). In addition, Mach number 3.0 (for which no experimental data were available) was

chosen to study the structures of supercritical flows where the centerbody shock falls inside the cowl lip and the flow is supersonic throughout the inlet flow field. For the computation of an inlet 'unstart' condition, Mach number 2.5 was chosen.

Computations and Code Performance

The flow fields considered for computations include the flow at supercritical without terminal shock, critical with terminal shock, and subcritical with a detached shock. Supercritical flow without a terminal shock is supersonic throughout the flow field, and the computations were impulsively started with a freestream initial condition imposed on all grid points. Throughout the computation, zero pressure gradient is maintained along the downstream boundary of the external zone and on the inlet exit surface (engine face). Critical flow with a terminal shock is supersonic upstream and subsonic downstream of the terminal shock wave which sits just downstream of the throat. These computations were impulsively started with a freestream condition imposed on all grid points located outside of the inlet. The starting conditions for the grid points in the inlet interior were linearly varied from the cowl lip at the freestream supersonic condition to a subsonic condition of approximately $\mathbf{M} = 0.6$ at the diffuser throat. From the diffuser throat to the engine face, the Mach number was set constant at $\mathbf{M} = 0.6$. As the computation was started, the static pressure at the inlet exit was raised gradually in the process of time iteration to a specified (experimentally measured) engine face pressure. At each time step, the total energy at the inlet exit was updated using the newly specified pressure and the velocity at the inlet exit that had been extrapolated from the interior grid points adjacent to the inlet exit. Subcritical flow is subsonic from the detached shock to the diffuser throat. The computations were impulsively started with a subsonic ($M_\infty = 0.8$) initial condition imposed on all grid points. In the process of time iteration, the freestream Mach number imposed on the upstream outer boundaries was raised gradually to a supersonic Mach number ($M_\infty = 2.5$). Throughout the computations, zero pressure gradient was maintained on the downstream boundary as in the case of supercritical and subcritical flow computations.

At each iteration in time, the surface pressure was computed from the normal momentum equation. A free stream condition was maintained on the upstream outer boundaries of the flow field throughout the process of integration in time. The computational results presented in this paper cover only an axisymmetric inlet, although the solver is capable of treating an inlet with an asymmetric configuration. The computations utilize a grid consisting of two zones with $138 \times 16 \times 49$ points per zone in the ξ, Θ, and η directions (Figure 1), respectively. Inviscid flow computations on the Ames Cray XMP/48 Computer required approximately 0.24 sec per iteration per zone for the axisymmetric inlet at zero angle of attack, and approximately 2.7 sec per iteration per zone for the axisymmetric inlet at an angle

of attack. The viscous computations took approximately 20% longer than the inviscid computations. The computation takes less than 1000 iterations to attain a converged solution.

Supercritical Flow Without a Terminal Shock

Figure 2a shows the computed inviscid Mach number contours for an axisymmetric inlet at $M_\infty = 3.0$ and $\alpha = 0$, and Figure 2b depicts the enlarged Mach contours of the inlet interior flow field. A centerbody shock wave is originated at the tip of the compression surface, and impinges inside the cowl lip. This shock is also reflected between the centerbody and cowl wall inside the inlet. From the cowl lip, a shock wave is originated toward the outer flow field. There is no shock wave from the cowl lip to the centerbody because the local flow angle is the same as the internal cowl angle. A compression wave is generated in the downstream region, $x \approx 5.5$, of the inlet flow field, owing to the abrupt change in the inlet geometry.

Figure 3a shows the Mach contours of the entire inviscid flow field at $M_\infty = 3.0$ and $\alpha = 5°$. The effects of flow incidence are shown in Figures 3b and 3c which depict the enlarged mach contours of the interior flow field at the windward and leeward planes of the inlet, respectively. The centerbody shock in the windward plane (Figure 3c) is closer to the centerbody than at $\alpha = 0°$ (Figure 2b), and interacts with the cowl expansion waves before impinging on and being reflected from the cowl surface. Two shock waves are present internally on the windward side of the inlet (Figure 3c); the upstream shock is the reflected shock originated from the centerbody, and the downstream shock is originated from the local curvature of the cowl inner surface. On the leeward side (Figure 3a), the centerbody shock falls farther upstream of the cowl lip inducing flow slippage in the lip region of the cowl. Internally on the leeward side of the inlet, a shock is present originating from the cowl lip.

Critical Flow With a Terminal Shock

Figure 4a shows the computed inviscid Mach contours of a critical flow (inlet 'started' with a terminal shock wave) at $M_\infty = 2.65$ and $\alpha = 0$. Figure 4b and Figure 4c show the computed surface pressures, along with experimentally measured pressure data, on the centerbody and the cowl, respectively. An experimentally measured[28] engine face static pressure ratio, $p_e/p_\infty = 19$, is imposed in the computation as a boundary condition at the engine face. The experimental static pressure distributions were obtained for a bleed mass flow equal to 5.5% of the capture mass flow. The bleed condition was not accounted for in the computation. An abrupt rise in pressure, shown in both the computed and experimental results, indicates the presence of a shock at a location just downstream of the throat. The Mach contours

presented in Figure 4a show a flow which is supersonic upstream and subsonic downstream of the shock. Upstream of the shock, the flow compresses supersonically up to the throat, and then expands from the throat to the shock. The computed throat shock is positioned downstream of the experimental throat-shock position owing to the viscous effects not being assumed in the computation.

Subcritical Flow

Figure 5a shows the computed Mach contours of an inviscid subcritical flow (inlet 'unstarted') at $M_\infty = 2.5$ and $\alpha = 0$, and Figure 5b depicts the enlarged Mach contours of the inlet flow field. In this case the shock is positioned upstream of the cowl lip, and subsonic flow spillage takes place in the region between the detached shock and the cowl lip. Thus, the flow condition is subsonic from the detached shock to the throat, an 'unstarted' inlet flow condition. Either an increase in freestream Mach number or an increase in throat area is required to restart the inlet.

Viscous Flow

Viscous effects on inlet flow were studied by computing the supercritical flow case (no terminal shock) using the Baldwin-Lomax algebraic turbulence model.[29] Figure 6a and Figure 6b show the results of viscous computations where the flow conditions, $M_\infty = 3.0$ and $\alpha = 0$, are the same as for the inviscid results in Figure 2. Unlike the external flow, the inlet flow is greatly influenced by the boundary layer, whose thickness is significant relative to the inlet geometry. This is evidenced in Figure 6 by a large Mach number gradient across the boundary layer near the inlet wall. The Mach contour distribution in viscous flow (Figure 6b) is less clustered than that in inviscid flow (Figure 2b), indicating that the shocks are smeared because of the presence of the boundary layer. Also the effective inlet throat area is smaller and the throat Mach number is lower because of the presence of boundary layer.

Conclusion

A new computational method was developed that extends the scope of inlet aerodynamic prediction over a variety of flow conditions.

The method was used to compute the external and internal flow field for a mixed compression axisymmetric inlet model. Results were obtained, at 0° angle of attack, for supercritical flow conditions without a terminal shock wave, critical condition with a terminal shock (inlet 'started'), and subcritical condition with the inlet at 'unstarted' condition. In addition, the flow fields were computed for supercritical flow condition at an angle of attack of 5°. Some of these computations

were compared with experimental results obtained from wind tunnel tests of an inlet model with the same contours but those tests employed boundary layer bleed.

The computations and experimental results compare reasonably well. The significant difference is in the location of the terminal shock wave; it is farther upstream for the experimental results because of the presence of the boundary layer.

Overall, the computer code works well, but a fully viscous computational method is needed for the simulation of complex inlet flow fields.

References

[1]Sorensen, V. L.,"Computer Program for Calculating Flow Fields in Supersonic Inlets," NASA TN D-2897, 1965.

[2]Reyhner, T. A., and Hickcox, T. E.,"Combined Viscous-Inviscid Analysis of Supersonic Inlet Flowfields," Journal of Aircraft, Vol.9, Aug. 1972, pp.589-595.

[3]Anderson, B. H., Tassa, Y., and Reshotko, E.,"Characteristic Procedure for Supersonic Flows Including Consideration for Viscous Contributions to Flow Rotationality," AIAA Paper 76-476, 1976.

[4]Vadyak, J., and Hoffman, J. D.,"Calculation of the Flow Fields in Supersonic Mixed-Compression Inlets at Angle of Attack Using the Three-Dimensional Method of Characteristics with Discrete Shock Wave-Fitting," NASA CR-135425, 1978.

[5]Vadyak, J., Hoffman, J. D. and Bishop, A. R.,"Three-Dimensional Flow Simulations for Supersonic Mixed-Compression Inlets at Incidence," AIAA Journal, Vol.22, No.7, July 1984, pp.873-881.

[6]Paynter G. C., and Chen, H. C.,"Progress Toward the Analysis of Supersonic Inlet Flows," AIAA 83-1371, 1983.

[7]Arlinger, B. G.,"Calculation of Transonic Flow Around Axisymmetric Inlets," AIAA Journal, Vol.13, Dec. 1975, pp. 1614-1621.

[8]Caughey, D. A., and Jameson, A.,"Accelerated Iterative Calculation of Transonic Nacelle Flowfields," AIAA Journal, Vol.15, No.10, Oct. 1977, pp.1474-1479.

[9]Reyhner, T. A.,"Cartesian Mesh Solution for Axisymmetric Transonic Potential Flow Around Inlets," AIAA Journal, Vol.15, May 1977, pp.624-631.

[10]Reyhner, T. A.,"Transonic Potential Flow Around Axisymmetric Inlets and Bodies at Angle-of-Attack," AIAA Journal, Vol.15, Sept. 1977, pp.1299-1306.

[11]Chen, L. T., and Caughey, D. A.,"Calculation of Transonic Inlet Flowfields Using Generalized Coordinates," J. of Aircraft, Vol.17, No.3, March 1980, pp.167-174.

[12]MacCormack, R. W.,"The Effect of Viscosity in Hypervelocity Impact Cratering," AIAA Paper 69-354, 1969.

[13]Presley, L. L.,"Internal Flow Calculations for Axisymmetric Supersonic Inlets at Angle of Attack," AIAA Paper 75-1214, 1975.

[14]Buggeln, R. C., McDonald, H., Kreskovsky, J. P., and Levy, R.,"Computation of Three-Dimensional Viscous Supersonic Flow in Inlets," AIAA Paper 80-0194, 1980.

[15]Knight D. D.,"Numerical Simulation of Realistic High-Speed Inlets Using the Navier-Stokes Equations," AIAA Journal, Vol.15, No.11, Nov. 1977, pp.1583-1589.

[16]Hunter, L. G., Tripp, J. M., and Howlett, D. G.,"A Mach 2.0 Plus Supersonic Inlet Study Using the Navier-Stokes Equations," AIAA Paper 85-1211, 1985.

[17]Campbell, A. F., and Forester, C. K., "Evaluation of a Method for Analyzing the Aperture Region of Two-Dimensional External Compression Inlets," AIAA Paper 85-3072, 1985.

[18]Kumar, A.,"Numerical Simulation of Flow Through Scramjet Inlets Using A Three-Dimensional Navier-Stokes Code," AIAA Paper 85-1664, 1985.

[19]Howlett, D. G., and Hunter, L. G.,"A Study of a Supersonic Axisymmetric Spiked Inlet at Angle of Attack Using the 3-D Navier-Stokes Equations," AIAA Paper 86-0308, 1986.

[20]Beam, R., and Warming, R. F.,"An Implicit Factored Scheme for the Compressible Navier-Stokes Equations," AIAA Paper 77-645, 1977.

[21]Steger, J. L.,"Implicit Finite-Difference Simulation of Flow About Arbitrary Two-Dimensional Geometries," AIAA journal, Vol.16, July 1978, pp.679-686.

[22]Chaussee, D. S., and Pulliam, T. H.,"Two-Dimensional Inlet Simulation Using a Diagonal Implicit Algorithm," AIAA Journal, Vol.19, No.2, Feb. 1981.

[23]Bush, R. H.,"External Compression Inlet Predictions Using An Implicit, Upwind, Multiple Zone Approach," AIAA Paper 85-1521, 1985.

[24]Coakley, T. J., and Hsieh, T.,"A Comparison Between Implicit and Hybrid Methods for the Calculation of Steady and Unsteady Inlet Flows," AIAA Paper 85-1125, 1985.

[25]Chyu, W. J., and Davis, S. S.,"Numerical Studies of Unsteady Transonic Flow Over An Oscillating Airfoil," AGARD Conference Proceedings No.374, 1984.

[26]Sorenson, R. L., and Steger, J. L.,"Simplified Clustering of Nonorthogonal Grids Generated by Elliptic Partial Differential Equations," NASA TM-73252, 1977.

[27]Thompkins, W. T., and Bush, R. H.,"Boundary Treatments for Implicit Solutions to Euler and Navier-Stokes Equations," Journal of Computational Physics, Vol.48, 1982, pp.302-311.

[28]Smeltzer, D. B., and Sorensen, N. E.,"Test of a Mixed Compression Axisymmetric Inlet With Large Transonic Mass Flow At Mach Numbers 0.6 To 2.65," NASA TN D-6971, 1972.

[29]Baldwin, B. S., and Lomax, H.,"Thin Layer Approximation and Algebraic Model for Separated Turbulent Flows," AIAA Paper 78-257, 1978.

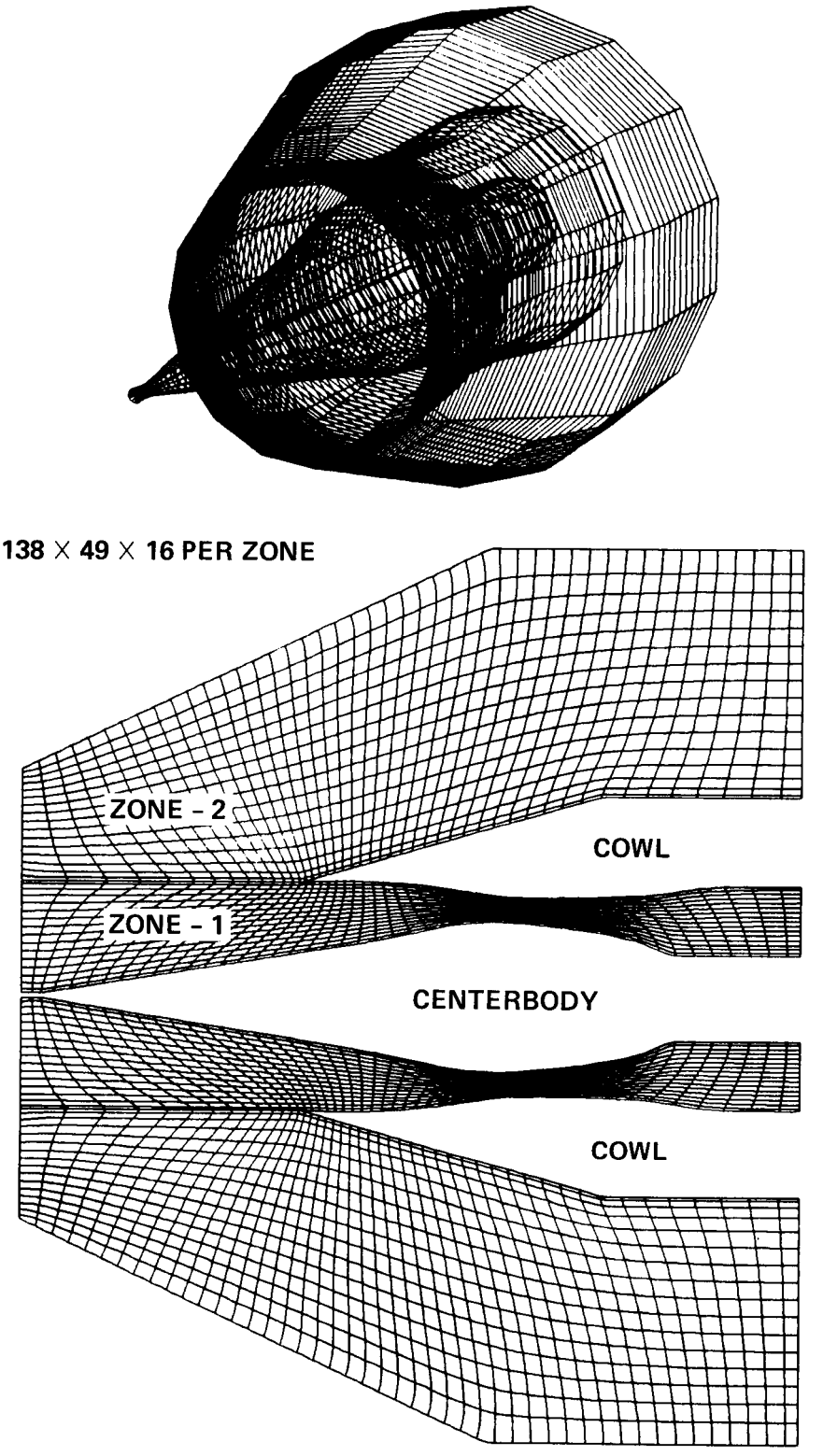

Figure 1.– Computational grid (not all grids are shown).

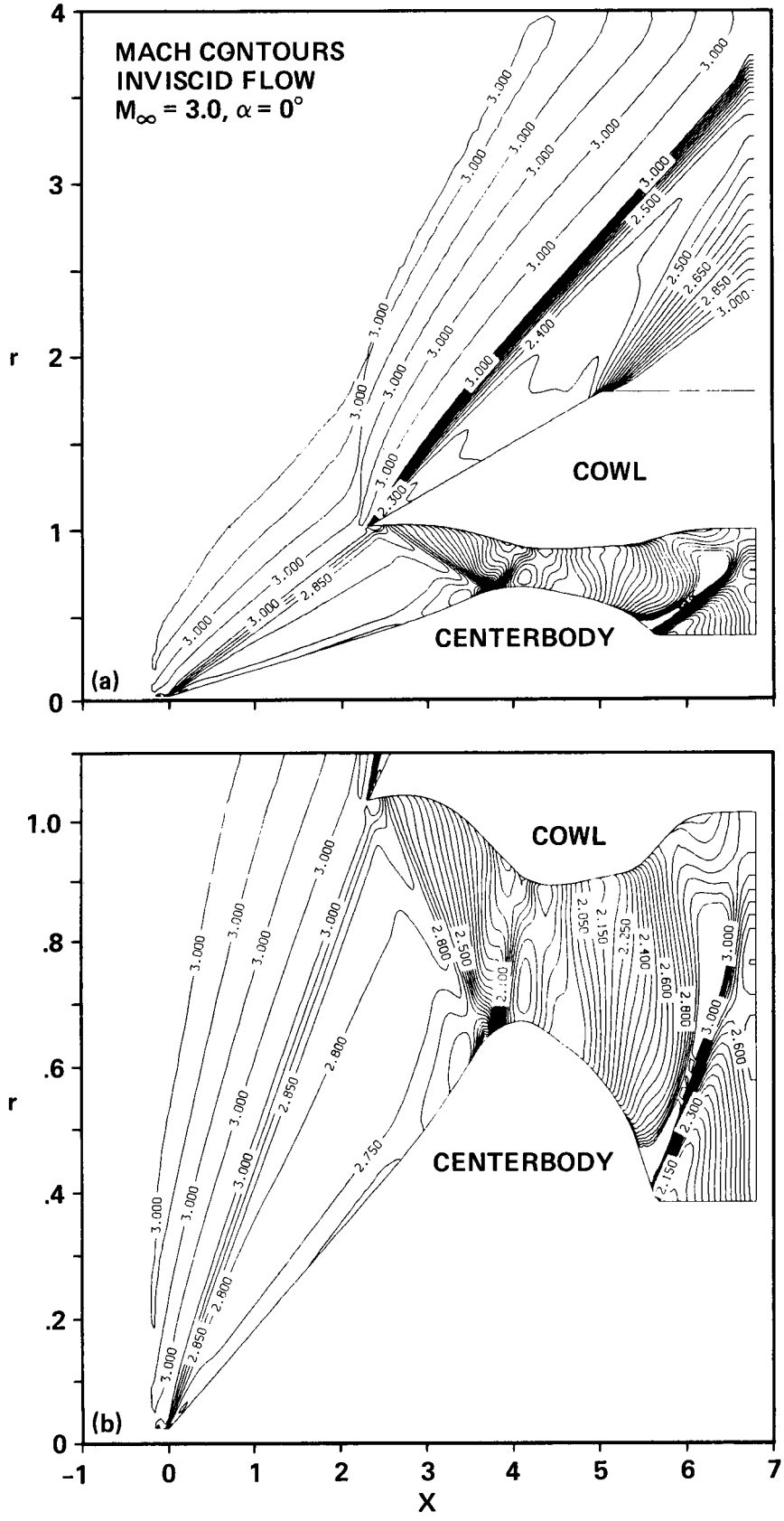

Figure 2.– Supercritical flow without terminal shock. (a) Overall flow field. (b) Enlarged inlet flow field.

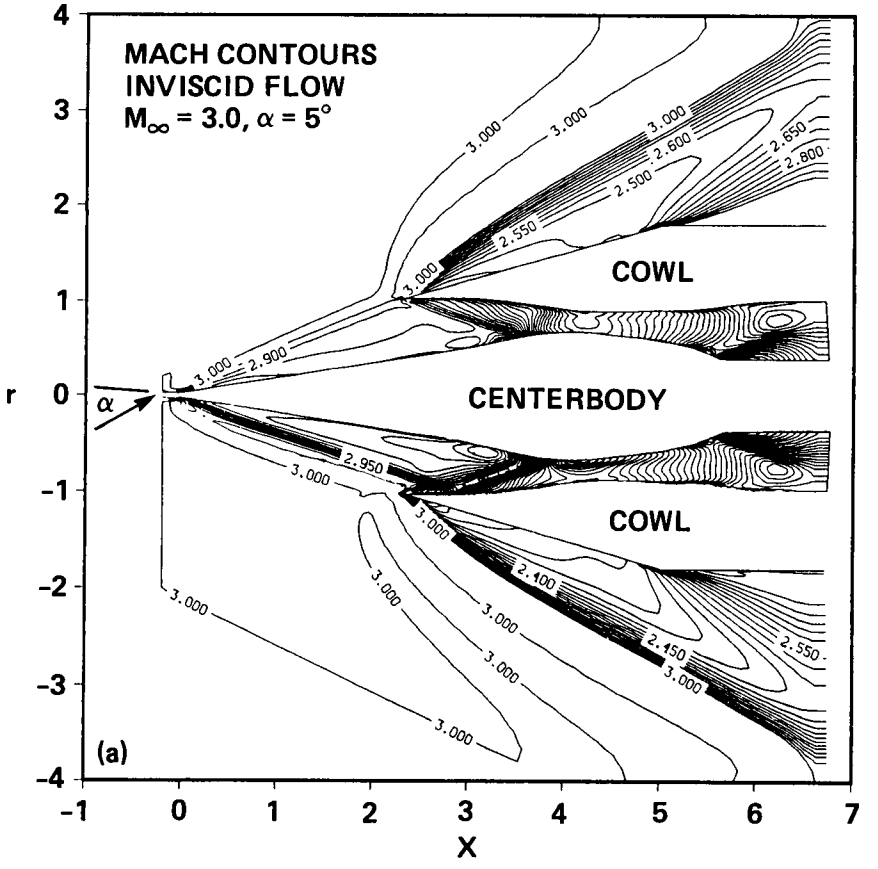

Figure 3.– Supercritical flow without terminal shock – effects of flow incidence. (a) Overall flow field.

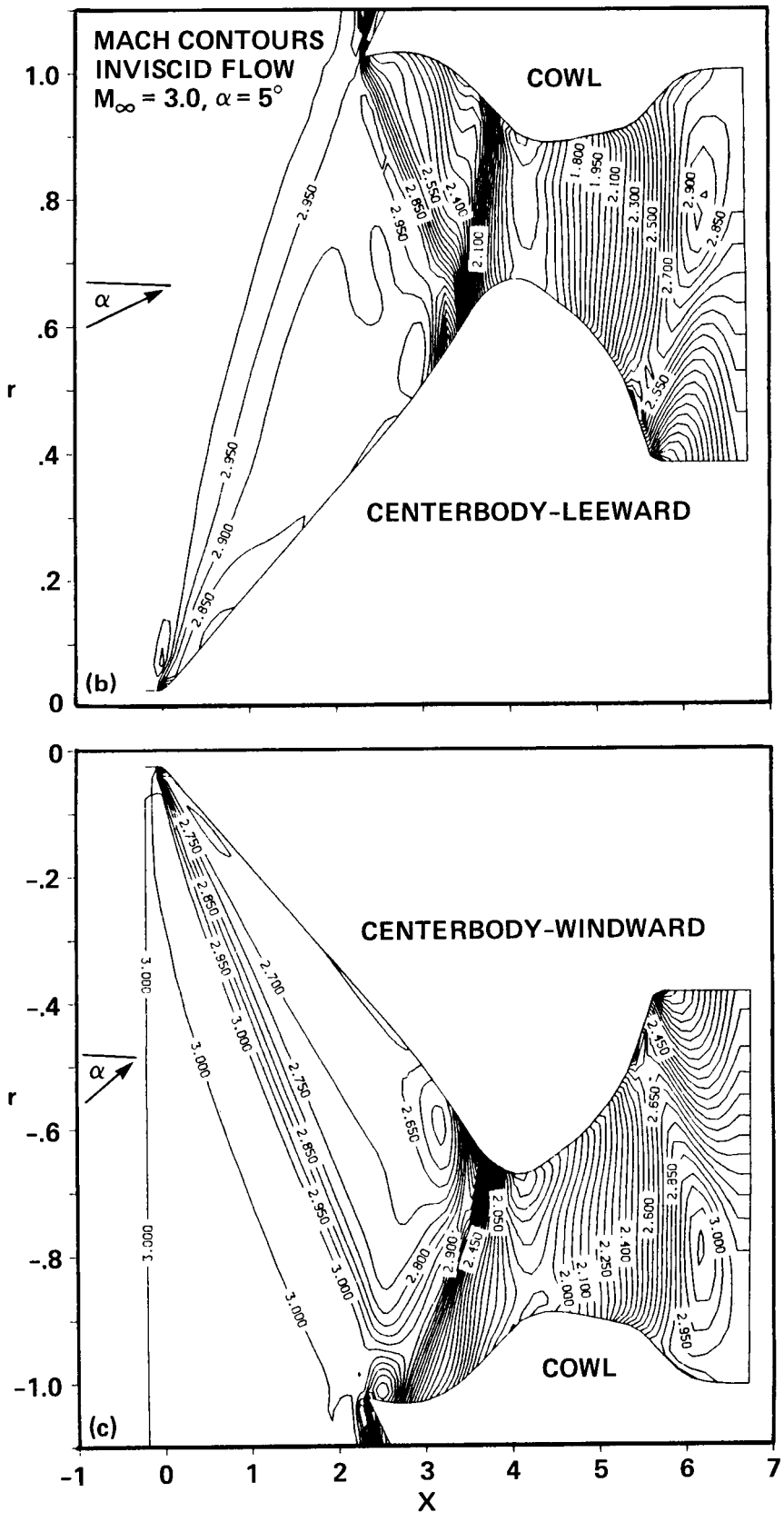

Figure 3.– Concluded. (b) Flow field in leeward plane. (c) Flow field in windward plane.

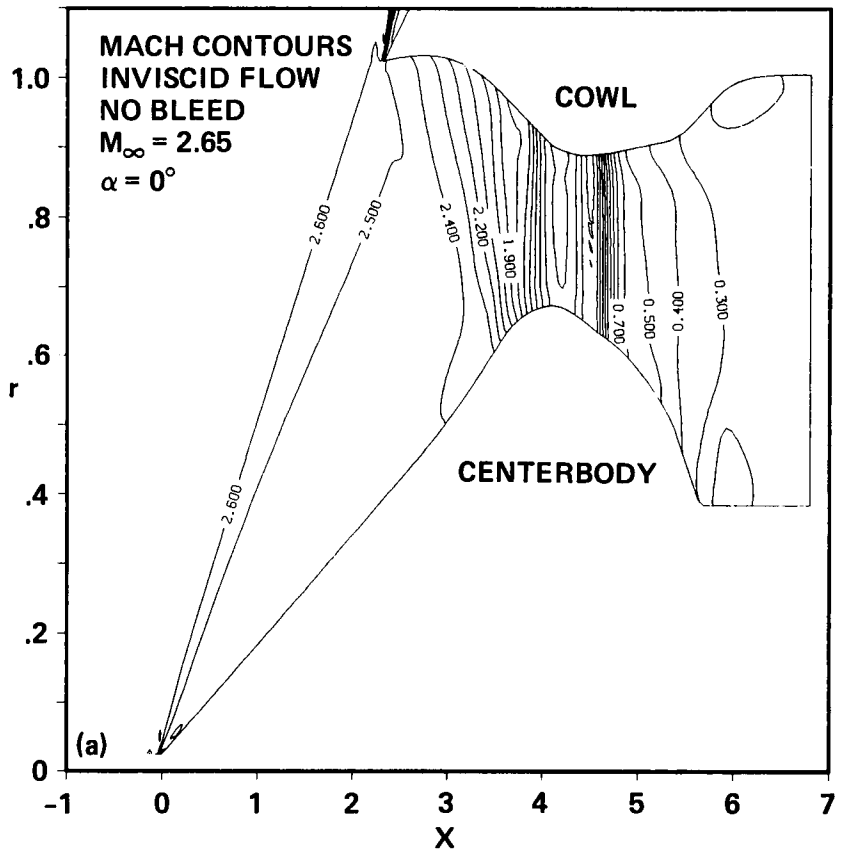

Figure 4.— Critical flow with terminal shock — inlet 'started' condition. (a) Mach contours.

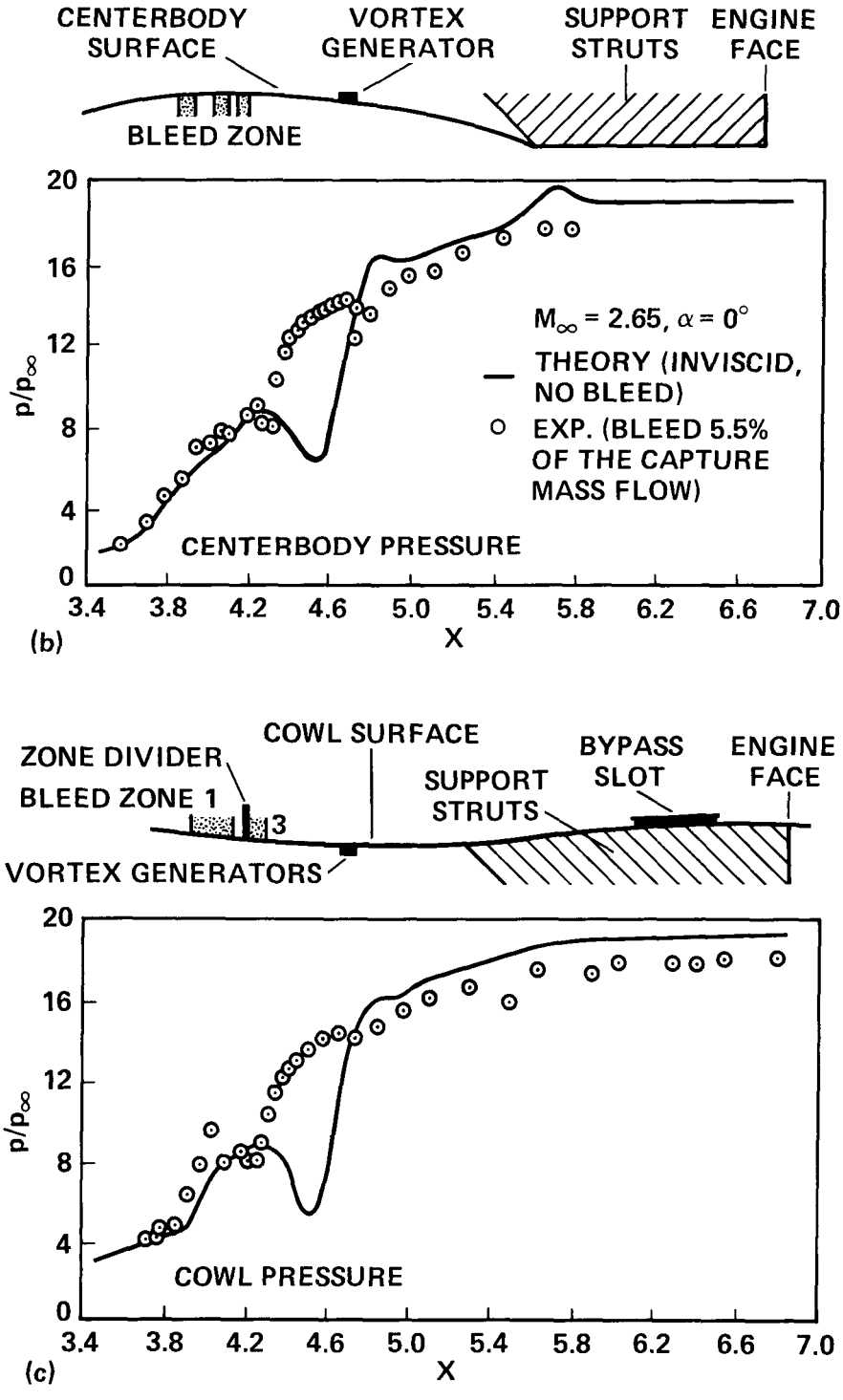

Figure 4.– Concluded. (b) Surface pressure on the centerbody. (c) Surface pressure on the cowl.

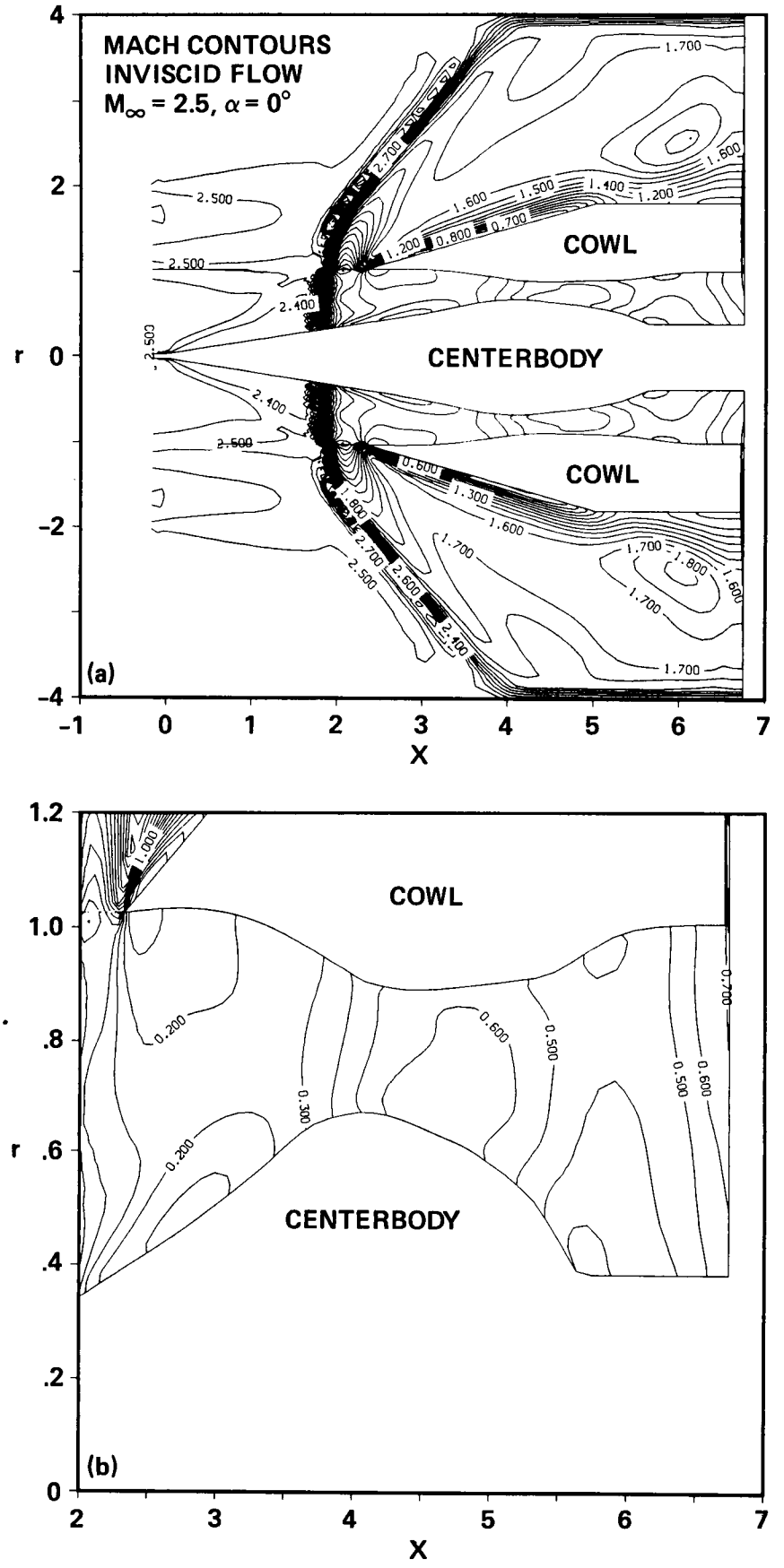

Figure 5.– Subcritical flow – inlet 'unstarted' condition. (a) Overall flow field. (b) Enlarged inlet flow field.

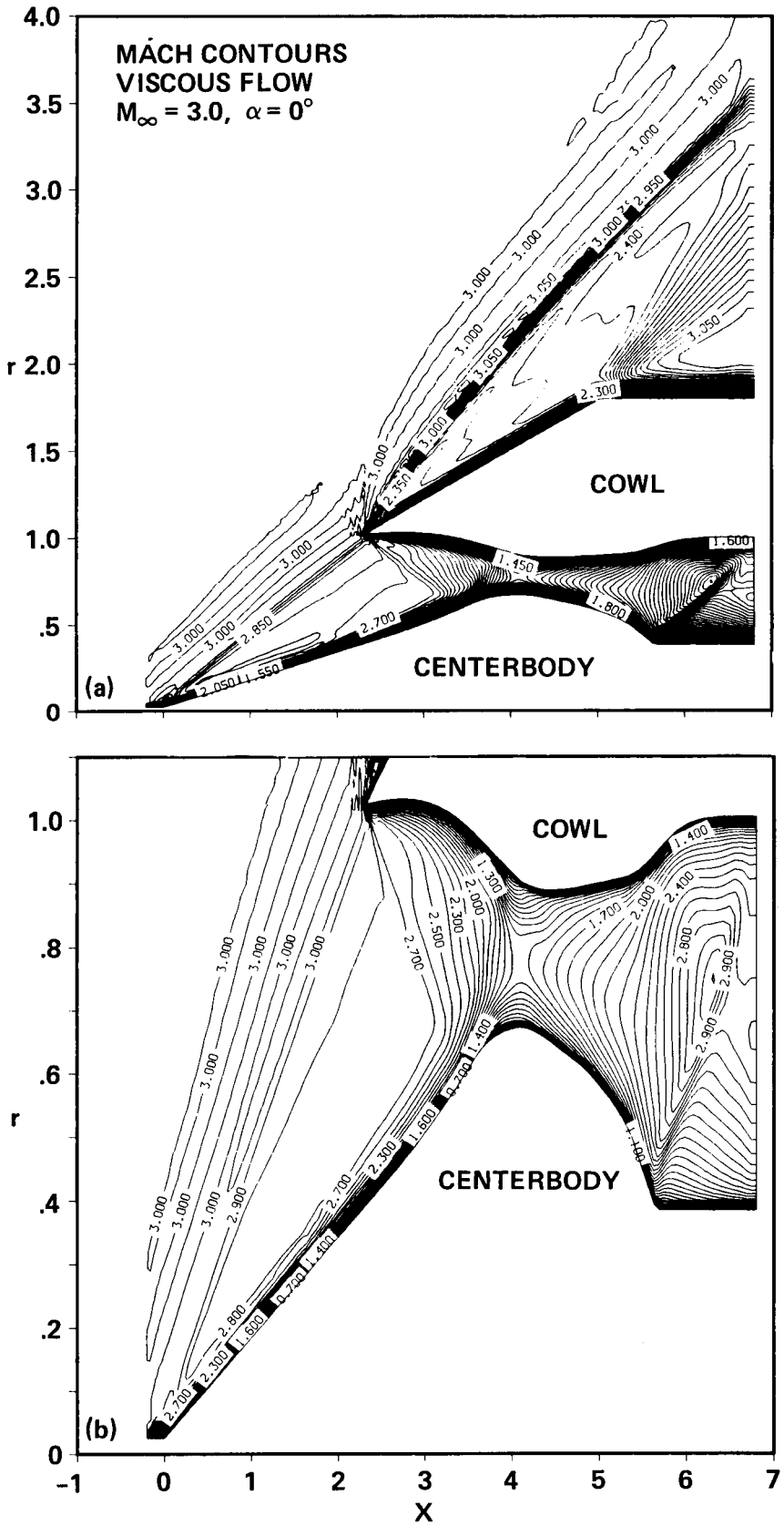

Figure 6.– Supercritical flow without terminal shock – viscous effects. (a) Overall flow field. (b) Enlarged inlet flow field.

1. Report No.	2. Government Accession No.	3. Recipient's Catalog No.
NASA TM 88362		

4. Title and Subtitle	5. Report Date
CALCULATION OF EXTERNAL-INTERNAL FLOW FIELDS FOR MIXED-COMPRESSION INLETS	October 1986
	6. Performing Organization Code
7. Author(s)	8. Performing Organization Report No.
W. J. Chyu, T. Kawamura, and D. P. Bencze	A-86409
	10. Work Unit No.
9. Performing Organization Name and Address	
Ames Research Center Moffett Field, CA 94035	11. Contract or Grant No.
	13. Type of Report and Period Covered
12. Sponsoring Agency Name and Address	Technical Memorandum
National Aeronautics and Space Administration Washington, DC 20546	14. Sponsoring Agency Code 505-60-21

15. Supplementary Notes

Point of Contact: W. J. Chyu, MS 227-6, Ames Research Center, Moffett Field, CA 94035
(415)694-6208 or FTS 464-6208

16. Abstract

Supersonic inlet flows with mixed external-internal compressions were computed using a combined implicit-explicit (Beam-Warming-Steger/MacCormack) method for solving the three-dimensional unsteady, compressible Navier-Stokes equations in conservation form. Numerical calculations were made of various flows related to such inlet operations as the shock-wave intersections, subsonic spillage around the cowl lip, and inlet 'started' versus 'unstarted' conditions. Some of the computed results were compared with wind tunnel data.

17. Key Words (Suggested by Author(s))	18. Distribution Statement
Inlet aerodynamics, Supersonic inlet, Navier-Stokes inlet code, Inlet 'started' flow, Mixed external/internal compression inlet, Combined implicit-explicit method	Unlimited Subject category – 02

19. Security Classif. (of this report)	20. Security Classif. (of this page)	21. No. of Pages	22. Price*
Unclassified	Unclassified	23	A02

*For sale by the National Technical Information Service, Springfield, Virginia 22161